Low-Damping Ferromagnetic Resonance in Electron-Beam Patterned, High-Q Vanadium Tetracyanoethylene Magnon Cavities

Andrew Franson,[1] Na Zhu,[2] Seth Kurfman,[1] Michael Chilcote,[1] Denis R. Candido,[3,4] Kristen S. Buchanan,[5] Michael E. Flatté,[3,4] Hong X. Tang,[2] and Ezekiel Johnston-Halperin[1]

[1)] *Department of Physics, The Ohio State University, Columbus, Ohio 43210, USA*

[2)] *Department of Electrical Engineering, Yale University, New Haven, Connecticut 06511, USA*

[3)] *Department of Physics and Astronomy, University of Iowa, Iowa City, Iowa 52242, USA*

[4)] *Pritzker School of Molecular Engineering, University of Chicago, Chicago, Illinois 60637, USA*

[5)] *Department of Physics, Colorado State University, Fort Collins, Colorado 80523, USA*

(Dated: 17 February 2022)

Integrating patterned, low-loss magnetic materials into microwave devices and circuits presents many challenges due to the specific conditions that are required to grow ferrite materials, driving the need for flip-chip and other indirect fabrication techniques. The low-loss ($\alpha = (3.98 \pm 0.22) \times 10^{-5}$), room-temperature ferrimagnetic coordination compound vanadium tetracyanoethylene ($V[TCNE]_x$) is a promising new material for these applications that is potentially compatible with semiconductor processing. Here we present the deposition, patterning, and characterization of $V[TCNE]_x$ thin films with lateral dimensions ranging from 1 micron to several millimeters. We employ electron-beam lithography and liftoff using an aluminum encapsulated poly(methyl methacrylate), poly(methyl methacrylate-methacrylic acid) copolymer bilayer (PMMA/P(MMA-MAA)) on sapphire and silicon. This process can be trivially extended to other common semiconductor substrates. Films patterned via this method maintain low-loss characteristics down to 25 microns with only a factor of 2 increase down to 5 microns. A rich structure of thickness and radially confined spin-wave modes reveals the quality of the patterned films. Further fitting, simulation, and analytic analysis provides an exchange stiffness, $A_{ex} = (2.2 \pm 0.5) \times 10^{-10}$ erg/cm, as well as insights into the mode character and surface spin pinning. Below a micron, the deposition is non-conformal, which leads to interesting and potentially useful changes in morphology. This work establishes the versatility of $V[TCNE]_x$ for applications requiring highly coherent magnetic excitations ranging from microwave communication to quantum information.

Interest in low-loss magnetic thin films has been growing due to potential applications in magnonics and quantum information as well as the potential for compact, high-efficiency magnetoelectric devices.[1–3] In the field of magnonics and spintronics, yttrium iron garnet ($Y_3Fe_5O_{12}$, YIG), an electrically insulating ferrite that exhibits extremely low Gilbert damping, $\alpha \approx 6 \times 10^{-5}$ and a linewidth of 3.4 G at 9.6 GHz for pristine nanometer-thick films, is currently the leading material for magnetoelectronic circuits.[4,5] The low-damping present in YIG films has led to its incorporation in magnetoelectric circuits and it also plays a prominent role in the study of magnonics research.[2,6–9] Patterning of YIG, however, presents a challenge. When patterned, the damping increases to $\alpha \approx 4 \times 10^{-4}$ to 8.74×10^{-4} for ion-milled films,[10,11] and $\alpha \approx 2.9 \times 10^{-4}$ to 5×10^{-4} for liftoff-based films.[12–14] Furthermore, post-growth annealing steps at temperatures as high as 850 °C are generally required to attain even these degraded damping values, and the lowest damping values are only achieved for films deposited on the lattice-matching substrate gadolinium gallium garnet ($Gd_3Ga_5O_{12}$, GGG), both of which provide strict limits on direct integration with functional devices.[15–17] Vanadium tetracyanoethylene ($V[TCNE]_x$, $x \approx 2$), on the other hand, is a low-loss (sub-Gauss linewidth at 9.83 GHz), room-temperature ($T_c = 600$ K) ferrimagnet that can be deposited optimally at 50 °C and 30 mmHg without the need for lattice matching.[18,19] These relatively benign deposition conditions allow for deposition on a wide variety of substrates and pre-patterned circuits, positioning $V[TCNE]_x$ as an exciting option for on-chip magnetic and magnonic device incorporation.[20–22] However, realizing this promise has been limited by the lack of techniques for patterning $V[TCNE]_x$ films at micron to sub-micron length scales.

Here we present a method for depositing and patterning $V[TCNE]_x$ using standard electron-beam lithography techniques with additional steps to preserve its high T_c and low-loss characteristics. The primary hurdles to micron-scale pattering of $V[TCNE]_x$ are its sensitivity to oxygen and solvents traditionally used in fabrication. Our past work has addressed air-sensitivity via encapsulation in a commercial organic light-emitting diode (OLED) epoxy, increasing its lifetime in air from hours to months,[23] and there are other commercial options, such as potting,[24] that promise to protect films indefinitely. This leaves solvent sensitivity, which inhibits the use of traditional patterning techniques for two reasons: i) the presence of solvent in the resist layer inhibits the deposition of $V[TCNE]_x$ as the solvent outgasses during growth, and ii) liftoff requires a solvent soak that will in general destroy or degrade the CVD-grown $V[TCNE]_x$ film. Here we address both of these challenges by using a thin AlO_x encapsulating layer for the resist and identifying a $V[TCNE]_x$-compatible solvent, respectively, demonstrating micron-scale patterning of $V[TCNE]_x$ films with no apparent increase in microwave loss. The patterned structures are characterized by scanning

electron microscopy (SEM) and by a combination of ferromagnetic resonance (FMR) and comparison with micromagnetic simulations and analytic calculations.

The CVD thin-film growth process typically results in a smooth blue-black $V[TCNE]_x$ film uniformly distributed across the substrate surface. When a resist is applied to the substrate before growth, however, $V[TCNE]_x$ deposition results in non-uniform coverage and poor $V[TCNE]_x$ quality. This is attributed to chemical reactions between the released solvents and the precursors (tetracyanoethylene and vanadium hexacarbonyl). Solvents present in common resists including LOR, MICROPOSIT S1800 series, and poly(methyl methacrylate) result in macroscopically inconsistent deposition of $V[TCNE]_x$ across the resist's surface as well as inside patterned areas. In order to address this solvent sensitivity, a 3 nm layer of aluminum is thermally deposited after development to encapsulate the resist layer. The aluminum is then oxidized with a ten-minute ultraviolet ozone clean in a UVOCS T10x10/OES prior to $V[TCNE]_x$ deposition.

In prior $V[TCNE]_x$ precipitation synthesis studies,[25–27] several solvents have been shown to precipitate $V[TCNE]_x$ with a modest impact on the T_c of the resulting powder. Since dichloromethane has a small impact on $V[TCNE]_x$ quality and readily dissolves poly(methyl methacrylate) (PMMA) and poly(methyl methacrylate-methacrylic acid 8.5%) (P(MMA 8.5 MAA)) at room temperature, this is the resist-solvent pair chosen to address the challenge of solvent based liftoff. Specifically, this work focuses on 495PMMA A6 on MMA (8.5) MAA EL 11 as a resist bilayer (PMMA/P(MMA 8.5 MAA)) to additively pattern low-loss $V[TCNE]_x$ onto sapphire, with the understanding that this patterning process should trivially extend to other inorganic substrates.[28,29]

Figure 1(a) shows the FMR response at 9.83 GHz of a $V[TCNE]_x$ thin film before and after a 2.5-hour soak in dichloromethane in a nitrogen atmosphere (< 10 ppm 0_2, < 2 ppm H_2O). The linewidth and lineshape of the resonance are largely unchanged, indicating that there is little to no incorporation of dichloromethane into the CVD-grown film on that timescale. The linewidth narrows slightly, possibly due to changes in the ordering of the $V[TCNE]_x$ due to solvent annealing.[30] The $V[TCNE]_x$ growth morphology that results from the above process is characterized by SEM and is shown in Fig. 1(b-c). Unlike physical vapor deposition, CVD deposition is driven by a combination of flow and diffusion. Figure 1(b) shows how the $V[TCNE]_x$ deposition is limited by the flow characteristics through the patterned features. In particular, $V[TCNE]_x$ does not form vertical sidewalls but rather forms gently sloped sidewalls at an angle of about 6° over a distance of approximately a micron from the edge. This leads to a parabolic profile, as one would expect from the velocity profile resulting from laminar flow through a channel, Fig. 1(c). These results suggest that there are likely opportunities to tune the structure profile by controlling channel width, flow direction, resist height, and resist morphology. This cross-sectional profile is difficult to achieve with other material systems and deposition techniques,[31] and it may prove beneficial for studies of spin-wave confinement as it offers a means to realize an approximation of an adiabatic boundary.

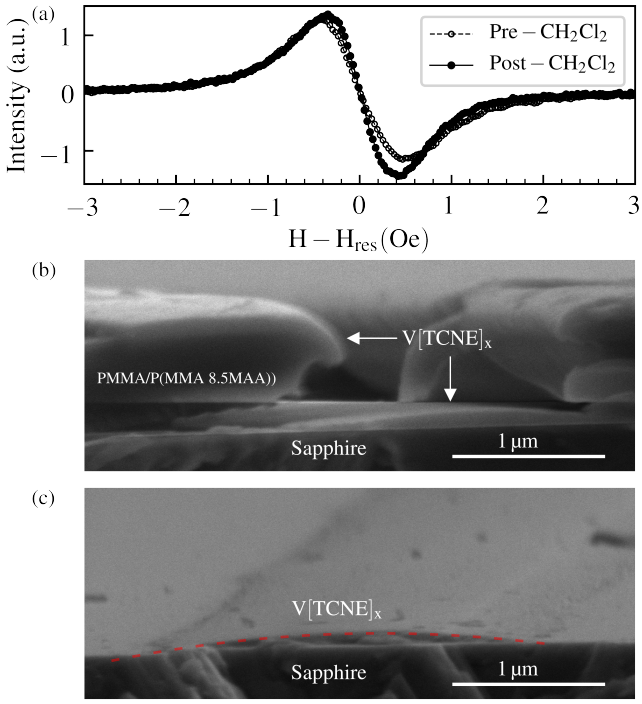

FIG. 1. (a) $V[TCNE]_x$ thin film FMR at 9.83 GHz and resonant field of 3565 Oe before and after a 2.5-hour soak in dichloromethane (CH_2Cl_2). SEM images of patterned $V[TCNE]_x$ film morphology before (b) and after (c) liftoff with dichloromethane reveal a parabolic deposition morphology into a 2 µm wide channel. The parabolic cross-section is highlighted with a dashed red line in (c).

Flow-limited deposition can, in principle, also lead to anisotropy in patterned features based on alignment between the flow direction and internal structure. Figure 2 shows various patterned structures of $V[TCNE]_x$ that are designed to explore these effects. The images show that there is anisotropic growth for several of the structures. The deposition time for these samples is 1.0 hr, leading to a nominal thickness of 300 nm. All shapes in Fig. 2 have a faint outline that reveals the ballistically deposited AlO_x layer. In Figs. 2(g, j), a dashed black semi-circle has been superimposed over the AlO_x outline to make it easier to compare the AlO_x and $V[TCNE]_x$ morphology. The outline shows that there is little to no offset or ellipticity present in the patterned 10 µm diameter $V[TCNE]_x$ disk. Figure 2(h), however, shows significant anisotropy as measured by the differences between the faint AlO_x outline and the $V[TCNE]_x$ pattern. The flow direction across the shape is left to right with a 20° tilt towards the top. The flow direction manifests in a more complete, laminar profile along the top and bottom whereas eddies inhibit deposition in the left and right interior edges. Laminar flow over a step predicts an eddy approximately as wide as the step is tall.[32,33] This is consistent with the fact that the 540 nm thick PMMA/P(MMA 8.5 MAA)) bilayer results in a roughly 500 nm wide region of reduced flow which leads to a taper in the morphology. This effect is also seen in Figs. 2(c, f) where the concave features at the corners see a reduction in deposition roughly 800 nm

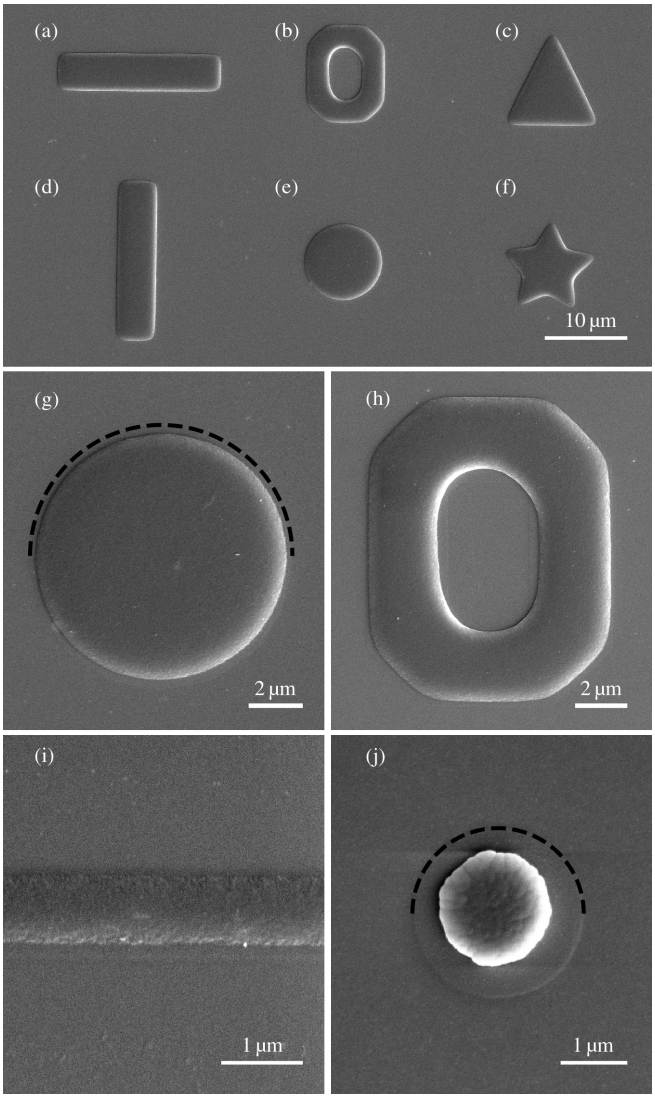

FIG. 2. Top view SEM images of various $V[TCNE]_x$ patterns after a 1.0 hr growth, about 300 nm thick. (a-f) Deposition morphology of several shapes with various features ranging from concave to convex to antidot. (g-h) Enhanced views of (e) and (b), respectively, show that flow-induced anisotropy is present in the complex Block O shape (h). (i-j) For features of order 1 micron or smaller, the restricted flow begins to affect the pattern deposition. The black, dashed semicircles in (g) and (j) highlight the AlO_x profile that is present for all shapes.

away from the planned shape shown by each AlO_x peak.

Figures 2(i, j) further explore the impacts of length scale on gas flow and growth morphology using bars and disks. The 1 µm wide bar in Fig. 2(i) acts as a channel for gas flow, yielding a parabolic deposition profile similar to Fig. 1(b, c) across the shape and good filling of the ballistic profile when the thickness of the bar in Fig. 2(i) is about 200 nm thick. In contrast, the 1.77 µm diameter disk in Fig. 2(j) is visibly off-center, with a 100 nm offset towards the top-left of the AlO_x. The deposition morphology in Fig. 2(j) resembles the eddy flow structure from boundary-driven flow into a cavity with a depth-to-width ratio of one-third, suggesting that flow over the features is laminar and the resulting deposition shape and cross-section can be simulated from flow.[32,33] It may be possible to achieve smaller features by using thinner resist layers, or by choosing pattern geometries that intentionally channel the flow, but these approaches will be pattern specific and are beyond the scope of this work.

To explore the utility of this patterning technique for magnonic and magnetoelectric devices, the magnetization dynamics of these microstructures are studied using FMR. Measurements are performed at room temperature in a Bruker EPR spectrometer with the microwave frequency held near 9.83 GHz while the applied magnetic field is swept across the $V[TCNE]_x$ resonance. Scans are then repeated for multiple polar angles, θ, from out-of-plane ($\theta = 0^\circ$, OOP) to in-plane ($\theta = 90^\circ$, IP) and for multiple azimuthal angles, φ, from parallel to the x-axis ($\varphi = 0^\circ$) to perpendicular to the x-axis ($\varphi = 90^\circ$).

Figure 3 shows the results of FMR characterization of 1 µm wide bars aligned parallel to the x-axis and 5 µm diameter disks. The bars are spaced 20 µm center to center in a 1D array and the disks are spaced 40 µm center to center in a 2D, square array. The position of the uniform mode of the bars (red) and disks (blue) is tracked as a function of orientation in Figs. 3(b, c). The bars show a single-peaked resonance that varies from 3550 to 3630 Oe as the structures are rotated IP to OOP. The disks reveal a more complicated peak structure, that suggests standing spin-wave modes are present, Fig. 3(i), and exhibit a larger field difference between IP and OOP resonances. This difference is evident in Fig. 3(d) where the resonances are tracked through multiple high-symmetry directions, revealing the full anisotropy of these structures.

The formalism developed by Smit, Beljers, and Suhl[34–36] is used to model this anisotropy. A Cartesian coordinate system is defined with x parallel to the length, y parallel to the width, and z parallel to the thickness of the bars as shown in Fig. 3(a). By explicitly considering the Zeeman and magnetostatic contributions to the free energy, F, one derives the expression,[37,38]

$$F = -M_i H_i + \frac{1}{2} M_i N_{ij} M_j, \tag{1}$$

where H_i are the components of the applied magnetic field, M_i are the components of the magnetization, and N_{ij} are components of the demagnetizing tensor, which leads to shape anisotropy, with i, j, k defined with respect to pattern axes. Solving for harmonic solutions with respect to time and minimizing F with respect to θ and φ yields

$$\begin{aligned}\frac{\omega}{\gamma} = \{&[H - 4\pi M_s N_{OP}\cos(2\theta)] \\ &\times [H - 4\pi M_s N_{OP}\cos^2(\theta) - 4\pi M_s N_{IP}\cos(2\varphi)] \\ &-16\pi^2 M_s^2 N_{IP}^2 \cos^2(\theta)\cos^2(\varphi)\sin^2(\varphi)\}^{1/2},\end{aligned} \tag{2}$$

where

$$N_{OP} \equiv N_z - N_x\cos^2(\varphi) - N_y\sin^2(\varphi), \tag{3a}$$

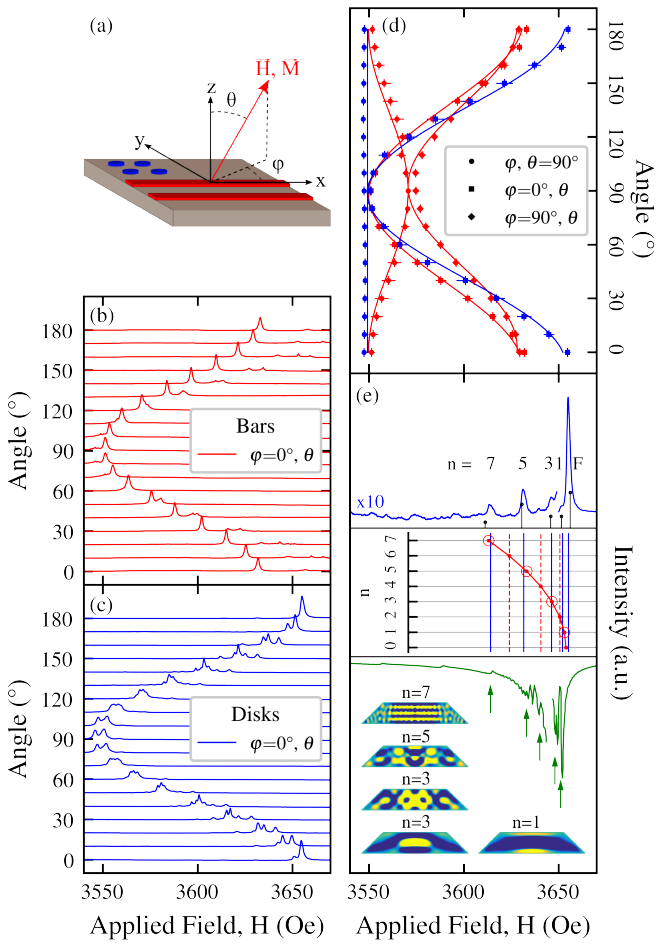

FIG. 3. Ferromagnetic resonance characterization of patterned V[TCNE]$_x$ bars and disks. (a) Schematic of the measurement geometry for the array of 1 µm bars (red) and 5 µm disks (blue) of V[TCNE]$_x$. (b-c) FMR response vs. applied field for $\theta = 0^\circ$ to $\theta = 180^\circ$ with φ fixed along the x-axis. (d) Uniform mode peak positions (symbols) for three high-symmetry directions and corresponding fit curves, Eq. 3. (e) Comparisons of experimental, analytic, and simulated OOP FMR spectra. OOP disk linescan (top, blue) with analytically calculated peak positions (top, black), thickness-mode fitting (middle, red), and micromagnetic simulations (bottom, green) with cross-sectional mode maps (bottom left, yellow and dark blue represent positive and negative motion, respectively, at an instant of time). Solid blue lines in middle panel indicate experimentally observed odd-mode resonance fields and the symbols show the best fit field values where the circled points (odd modes) were used for the fits. Red dashed lines show predicted even-mode resonances.

$$N_{IP} \equiv N_x - N_y, \tag{3b}$$

N_x, N_y, N_z are the diagonal components of the demagnetizing tensor, θ is the polar angle, and φ is the azimuthal angle that the sample magnetization makes with the pattern axes, Fig. 3(a). Equation 2 is derived assuming the demagnetizing field is parallel to the magnetization, so $N_{ij} = N_{ij}\delta_{ij} = N_i$, and that the magnetization, (θ_M, φ_M), is parallel to the applied field, (θ_H, φ_H), so only one set of angles is needed to describe the magnetization and applied field, (θ, φ). This approximation is validated by the fact that $4\pi M_s$ for V[TCNE]$_x$ is less than 95 G, and the applied magnetic fields used for these measurements are 3500 to 3750 Oe. As a result, $\vec{M}$ is parallel to $\vec{H}$ to within 1.5 degrees for the experiments shown here.

The other potential source of anisotropy is the crystal field which arises from the local coordination of the exchange interaction. For uniaxial crystal-field anisotropy, this crystal field can be decomposed into components acting along the pattern axes with the same angular dependence as the demagnetizing anisotropy. As a result, the N_i that are extracted from the fit to Eq. 2 are a combination of demagnetizing-field and crystal-field components with the form

$$A_i \equiv N_{i,extracted} = N_{i,demag} + \frac{H_{i,crystal}}{4\pi M_s}, \tag{4}$$

where A_i is the observed anisotropy tensor component, $N_{i,demag}$ is the geometric demagnetizing tensor component, and $H_{i,crystal}$ is the additional crystal field along that axis.

Three anisotropy tensors are used to determine the strength of the crystal field in the bars and the disks. The first, $A_{i,fit}$, is generated from simultaneous fits to the three red anisotropy curves in Fig. 3(d) from the bar array to Eq. 2. These fits yield $4\pi M_s = 76.57 \pm 1.67$ G and $|\frac{\gamma}{2\pi}| = 2.742 \pm 0.040$ MHz/Oe, which agree with literature values,[19,20] and $A_{x,fit} = 0.00 \pm 0.01$, $A_{y,fit} = 0.189 \pm 0.019$, and $A_{z,fit} = 0.707 \pm 0.026$. The trace of this anisotropy tensor is 0.896 ± 0.046, indicating the magnitude of the crystal-field contribution is 7.96 ± 2.47 Oe. Using SEM measurements to geometrically determine a pure demagnetizing tensor for the bars, $N^{bar}_{i,demag}$, that does not include crystal-field effects yields $N^{bar}_{x,demag} = 0$, $N^{bar}_{y,demag} = 0.21$, and $N^{bar}_{z,demag} = 0.79$.[39] Comparing the $A_{i,fit}$ with these $N^{bar}_{i,demag}$, the z direction shows the largest difference of 0.09, indicating this crystal field is oriented along the z-axis of the bars. The magnitude of this crystal field is consistent with previous measurements of V[TCNE]$_x$ templated nanowires.[22] In addition to being self-consistent, these results also predict the anisotropy curves for the disks (blue lines in Fig. 3(d)). To test these fitting results, a final demagnetizing tensor, $N^{disk}_{i,demag}$, for the disk are calculated as $N^{disk}_{x,demag} = N^{disk}_{y,demag} = 0.028$ and $N^{disk}_{z,demag} = 0.944$ based on SEM measurements and demagnetizing expressions from the literature.[40] Combining this with the $4\pi M_s$ and $|\frac{\gamma}{2\pi}|$ values from the previous fit results in the solid blue curves shown in Fig. 3(d) with a combined reduced chi-squared value of 0.96. Adding crystal-field effects degrades the quality of the reduced chi-squared value for $H^{disk}_{z,crystal} > 0.7$ Oe, indicating the absence of crystal-field effects in the disks. These results suggest the crystal-field contribution arises from anisotropic relaxation in the patterned bars, which corroborates prior work with V[TCNE]$_x$ nanowires where an additional in-plane crystal field is reported due to anisotropy in the relaxation of the templated structures.[22]

The more complicated spectra of the disks suggests that the disks are acting as spin-wave cavities with complex internal mode structure, Fig. 3(e). Numerical simulations and analytical calculations are carried out to better understand this mode structure. To begin characterizing the mode struc-

ture, the strongest experimental peaks are compared with the odd analytic thickness modes predicted for a thin film in the OOP geometry.[41] The vertical blue lines in Fig. 3(e) represent the experimental peak values. Fitting to these peak values using the mode assignments indicated in Fig. 3(e) and the parameters obtained from the FMR measurements yields the red analytic curve and a value of the exchange stiffness, $A_{ex} = (2.2 \pm 0.5) \times 10^{-10}$ erg/cm. The even thickness modes, shown as dashed red lines, agree well with smaller peaks within the experimental data. Analytic disk calculations shown in black in Fig. 3(e) further describe the identity of the quantum confined modes and agree well when using this A_{ex}. The exchange stiffness depends on M_s; an approximate form, found by several means,[42–44] is $A_{ex} \propto M_s^2$. The exchange length constant $\lambda_{ex} = \frac{2A_{ex}}{\mu_0 M_s^2}$ is therefore a better metric to use to compare samples with different saturation magnetizations. The difference between the exchange length from this study of $\lambda_{ex} = 9.7$ nm and the previously reported value of 21 nm[20] could be due to differences in grain structure between the patterned and unpatterned films[44] as well as difficulty in mode assignment, n, in prior work where fewer modes are visible.

Numeric modeling is performed using time-domain micromagnetic simulations with the open-source GPU-based software MuMax3 while using the material parameters determined from the fits to the experimental data.[45] The factors that have the most relevant influence on the simulated peak structure are (i) the sloped sidewalls that (a) have a strong effect on the shape of the lowest frequency set of peaks which are comprised of a set of closely-spaced radially and lowest-order thickness quantized modes and (b) apply an overall shift to the thickness confined modes, (ii) the pinning conditions of the surfaces that have a strong effect on the amplitudes of the thickness-confined modes, and (iii) the exchange stiffness, A_{ex}, that controls the spacing between thickness quantized modes. Sloped sidewalls are used in the simulations to replicate the shape that occurs due to the slower growth rate within 1 micron of the resist. The simulations show that the position of the most prominent peak relative to the thickness-confined modes is sensitive to the exact shape of the sidewalls and the pinning conditions. To account for small differences in the slope of simulated and experimental data, the higher-order thickness modes are aligned with experiment instead of the uniform mode in Fig. 3(e). Simulations with perfect pinning at the top and bottom surfaces agree better with the experimentally observed thickness and radial confined mode structure as compared to simulations with top, bottom, or no pinning; however, the close agreement between the calculated even-mode resonance fields and several smaller peaks in the experimental spectrum suggests that one of the surfaces likely has slightly weaker pinning than the other. Additional simulations can be found in the supplement. The resulting simulated frequency response of the simulation is in green in Fig. 3(e) along with several mode maps at peaks indicated by the green arrows. These maps reveal quantization in the thickness and radial directions in the tapered structure. The lower-order thickness modes each show distinct radial quantization. The $n = 7$ thickness mode, shows a nearly pure thickness quantization and represents the sum of multiple closely-spaced radials

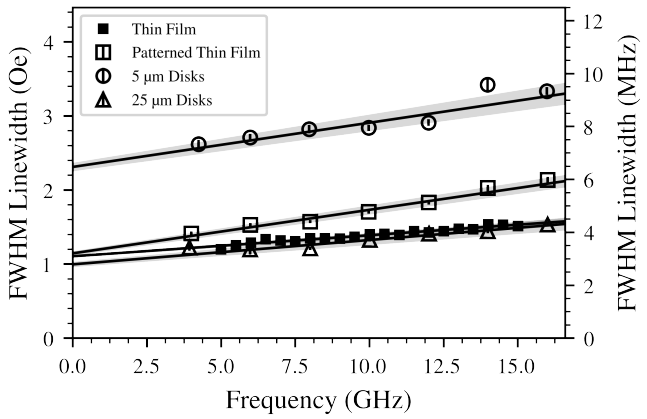

FIG. 4. Full-width at half-maximum linewidth vs resonant frequency for various $V[TCNE]_x$ pattern sizes from thin films to 5 μm diameter disks. All linewidths are extracted from the OOP geometry. All growths were 1-hour long, resulting in a 300 nm thick film for the 5 μm film and 400 nm thickness for the rest. The patterned thin film is a 2 mm by 2 mm patterned patch of $V[TCNE]_x$.

modes that are excited simultaneously. The agreement between simulated and experimental spectra demonstrates control over the spin-wave mode structure and lays the foundation for the study and application of magnon cavities with adiabatic boundaries and engineered mode structures.

In addition to analyzing anisotropy and mode structure, FMR can be used to determine the total magnetic loss, or damping of these magnon modes. This damping potentially contains both homogeneous and inhomogeneous sources as parameterized via the Gilbert damping factor, α.[46] The damping for the patterned $V[TCNE]_x$ films is measured via broadband ferromagnetic resonance (BFMR) performed in a custom built microstrip-based system wherein the applied magnetic field is held constant in the OOP geometry and the microwave frequency is swept across the $V[TCNE]_x$ resonance. Figure 4 shows the linewidth vs frequency extracted for representative samples of disks and unpatterned films, with vertical lines indicated the error in the fits. Representative raw data and fits can be found in the supplemental information. The Gilbert damping is fit using Suhl's expression for the full-width at half-maximum (FWHM) FMR linewidth,[34]

$$\Delta H = \frac{\alpha}{|d\omega_{res}/dH|}\frac{\gamma}{M}\left(F_{\theta\theta} + \frac{1}{\sin^2(\theta)}F_{\varphi\varphi}\right), \qquad (5)$$

in combination with phenomenological inhomogeneous broadening.[47] This results in

$$\Delta H = \frac{4\pi\alpha}{|\gamma|}f + \Delta H_0, \qquad (6)$$

when one uses $\theta = 0$ for the OOP geometry.[46] In Eq. 6, ΔH is the FWHM linewidth of the resonance, α is the Gilbert damping, and ΔH_0 is the FWHM contribution from inhomogeneous broadening. The fits yield $\alpha = (3.98 \pm 0.22) \times 10^{-5}$ for unpatterned films, $\alpha = (4.60 \pm 0.44) \times 10^{-5}$ for 25 μm features, and $\alpha = (8.34 \pm 0.77) \times 10^{-5}$ for 5 μm disks. The thin-film damping result of $(3.98 \pm 0.22) \times 10^{-5}$ places $V[TCNE]_x$

films comfortably alongside YIG films as the lowest magnetic damping material currently available, and the retention of that ultra-low damping after patterning is considerably better than the reported values for patterned YIG structures.[10–14] In addition to low-damping, the high-frequency measurements of the thin film and 25 µm disks have Quality (Q) factors, $\frac{f}{\Delta f}$, of over 3,700, competitive with Q factors for YIG thin films.[48] Retaining ultra-low damping and high Q in patterned $V[TCNE]_x$ for features as small as 25 µm and as large as millimeters, both relevant length scales for many magnonic cavity applications,[3,14,49–52] combined with the flexibility to deposit on most inorganic substrates, positions $V[TCNE]_x$ to complement YIG in magnonic and magnetoelectric devices where integration of GGG or high-temperature annealing steps is limiting, such as for small form factors and on-chip integration.

In summary, this work demonstrates a method for patterning the ferrimagnetic coordination compound vanadium tetracyanoethylene. Standard electron-beam lithography of PMMA/P(MMA-MAA) bilayers is used in conjunction with pre-growth aluminum encapsulation and post-growth dichloromethane liftoff to pattern $V[TCNE]_x$ thin films with no degradation of the microwave magnetic properties. The sidewalls of structures patterned in this way are sloped, allowing for the investigation and quantitative modeling of spin-wave confinement in magnetic structures with soft boundary conditions. Patterned $V[TCNE]_x$ films with features down to 25 µm exhibit a high Q of over 3,700 and ultra-low damping of $(4.60 \pm 0.44) \times 10^{-5}$ which are competitive with unpatterned YIG and lower than all existing reports of patterned YIG microstructures.[10–14] The versatility of the patterning and deposition conditions of $V[TCNE]_x$, in combination with its ultra-low magnetic damping, position $V[TCNE]_x$ as a promising candidate for incorporation into magnetoelectric devices where low-loss, highly coherent, magnon excitation are desirable. Such applications range from microwave communications to quantum information.

SUPPLEMENTARY MATERIALS

See supplementary material for the a detailed description of sample fabrication, measurement techniques, simulations, and analytic calculations.

ACKNOWLEDGMENTS

This work is supported by Emerging Frontiers in Research and Innovation (EFRI) Grant No. EFMA-1741666. The authors acknowledge the NanoSystems Laboratory at The Ohio State University.

[1] Y. Cheng, B. Peng, Z. Hu, Z. Zhou, and M. Liu, "Recent development and status of magnetoelectric materials and devices," Physics Letters A **382**, 3018–3025 (2018).

[2] A. Nikitin, A. Ustinov, A. Semenov, A. Chumak, A. Serga, V. I. Vasyuchka, E. Lahderanta, B. Kalinikos, and B. Hillebrands, "Width-modulated magnonic crystal and its application for spin-wave logic," 2015 European Microwave Conference (EuMC) (2015), 10.1109/eumc.2015.7345998.

[3] A. V. Chumak, A. A. Serga, and B. Hillebrands, "Magnonic crystals for data processing," Journal of Physics D: Applied Physics **50**, 244001 (2017).

[4] H. Chang, P. Li, W. Zhang, T. Liu, A. Hoffmann, L. Deng, and M. Wu, "Nanometer-thick yttrium iron garnet films with extremely low damping," IEEE Magnetics Letters **5**, 1–4 (2014).

[5] C. Hauser, T. Richter, N. Homonnay, C. Eisenschmidt, M. Qaid, H. Deniz, D. Hesse, M. Sawicki, S. G. Ebbinghaus, and G. Schmidt, "Yttrium iron garnet thin films with very low damping obtained by recrystallization of amorphous material," Scientific Reports **6** (2016), 10.1038/srep20827.

[6] A. A. Serga, A. V. Chumak, and B. Hillebrands, "YIG magnonics," Journal of Physics D: Applied Physics **43**, 264002 (2010).

[7] T. Schneider, A. A. Serga, B. Leven, B. Hillebrands, R. L. Stamps, and M. P. Kostylev, "Realization of spin-wave logic gates," Applied Physics Letters **92**, 022505 (2008).

[8] O. Zahwe, B. Abdel Samad, B. Sauviac, J. P. Chatelon, M. F. Blanc Mignon, J. J. Rousseau, M. Le Berre, and D. Givord, "Yig thin film used to miniaturize a coplanar junction circulator," Journal of Electromagnetic Waves and Applications **24**, 25–32 (2010).

[9] A. V. Chumak, "Magnon spintronics," Spintronics handbook: Spin transport and magnetism, second edition , 247–302 (2019).

[10] C. Hahn, V. V. Naletov, G. de Loubens, O. Klein, O. d' Allivy Kelly, A. Anane, R. Bernard, E. Jacquet, P. Bortolotti, V. Cros, and et al., "Measurement of the intrinsic damping constant in individual nanodisks of $Y_3Fe_5O_{12}$ and $Y_3Fe_5O_{12}$|Pt," Applied Physics Letters **104**, 152410 (2014).

[11] M. B. Jungfleisch, W. Zhang, W. Jiang, H. Chang, J. Sklenar, S. M. Wu, J. E. Pearson, A. Bhattacharya, J. B. Ketterson, M. Wu, and et al., "Spin waves in micro-structured yttrium iron garnet nanometer-thick films," Journal of Applied Physics **117**, 17D128 (2015).

[12] A. Krysztofik, L. E. Coy, P. Kuświk, K. Załęski, H. Głowiński, and J. Dubowik, "Ultra-low damping in lift-off structured yttrium iron garnet thin films," Applied Physics Letters **111**, 192404 (2017).

[13] S. Li, W. Zhang, J. Ding, J. E. Pearson, V. Novosad, and A. Hoffmann, "Epitaxial patterning of nanometer-thick $Y_3Fe_5O_{12}$ films with low magnetic damping," Nanoscale **8**, 388–394 (2016).

[14] N. Zhu, H. Chang, A. Franson, T. Liu, X. Zhang, E. Johnston-Halperin, M. Wu, and H. X. Tang, "Patterned growth of crystalline $Y_3Fe_5O_{12}$ nanostructures with engineered magnetic shape anisotropy," Applied Physics Letters **110**, 252401 (2017).

[15] M. C. Onbasli, A. Kehlberger, D. H. Kim, G. Jakob, M. Kläui, A. V. Chumak, B. Hillebrands, and C. A. Ross, "Pulsed laser deposition of epitaxial yttrium iron garnet films with low gilbert damping and bulk-like magnetization," APL Materials **2**, 106102 (2014).

[16] S. A. Manuilov and A. M. Grishin, "Pulsed laser deposited $Y_3Fe_5O_{12}$ films: Nature of magnetic anisotropy II," Journal of Applied Physics **108**, 013902 (2010).

[17] S. A. Manuilov, R. Fors, S. I. Khartsev, and A. M. Grishin, "Submicron $Y_3Fe_5O_{12}$ film magnetostatic wave band pass filters," Journal of Applied Physics **105**, 033917 (2009).

[18] M. Harberts, Y. Lu, H. Yu, A. J. Epstein, and E. Johnston-Halperin, "Chemical vapor deposition of an organic magnet, vanadium tetracyanoethylene," Journal of Visualized Experiments (2015), 10.3791/52891.

[19] H. Yu, M. Harberts, R. Adur, Y. Lu, P. C. Hammel, E. Johnston-Halperin, and A. J. Epstein, "Ultra-narrow ferromagnetic resonance in organic-based thin films grown via low temperature chemical vapor deposition," Applied Physics Letters **105**, 012407 (2014).

[20] N. Zhu, X. Zhang, I. H. Froning, M. E. Flatté, E. Johnston-Halperin, and H. X. Tang, "Low loss spin wave resonances in organic-based ferrimagnet vanadium tetracyanoethylene thin films," Applied Physics Letters **109**, 082402 (2016).

[21] H. Liu, C. Zhang, H. Malissa, M. Groesbeck, M. Kavand, R. McLaughlin, S. Jamali, J. Hao, D. Sun, R. A. Davidson, and et al., "Organic-based magnon spintronics," Nature Materials **17**, 308–312 (2018).

[22] M. Chilcote, M. Harberts, B. Fuhrman, K. Lehmann, Y. Lu, A. Franson, H. Yu, N. Zhu, H. Tang, G. Schmidt, and E. Johnston-Halperin, "Spin-wave confinement and coupling in organic-based magnetic nanostructures," (2019), arXiv:1901.03286v1 [cond-mat.mtrl-sci].

[23] I. H. Froning, M. Harberts, Y. Lu, H. Yu, A. J. Epstein, and E. Johnston-Halperin, "Thin-film encapsulation of the air-sensitive organic-based ferrimagnet vanadium tetracyanoethylene," Applied Physics Letters **106**, 122403 (2015).

[24] D. Bardoliwalla, "Fast curing, low exotherm epoxy potting and encapsulating systems," Proceedings: Electrical insulation conference and electrical manufacturing and coil winding conference 10.1109/eeic.1997.651053.

[25] M. S. Thorum, K. I. Pokhodnya, and J. S. Miller, "Solvent enhancement of the magnetic ordering temperature (T_c) of the room temperature $V[TCNE]_x \cdot S$ (S=solvent, TCNE=tetracyanoethylene; $x \approx 2$) magnet," Polyhedron **25**, 1927–1930 (2006).

[26] K. I. Pokhodnya, D. Pejakovic, A. J. Epstein, and J. S. Miller, "Effect of solvent on the magnetic properties of the high-temperature $V[TCNE]_x$ molecule-based magnet," Physical Review B **63** (2001), 10.1103/physrevb.63.174408.

[27] J. Zhang, J. S. Miller, C. Vazquez, P. Zhou, W. B. Brinckerhoff, and A. J. Epstein, "Improved synthesis of the $V(\text{tetracyanoethylene})_x \cdot y(\text{solvent})$ room-temperature magnet: Doubling of the magnetization at room temperature," Molecule-Based Magnetic Materials , 311–318 (1996).

[28] A. Tseng, K. Chen, C. Chen, and K. Ma, "Electron beam lithography in nanoscale fabrication: Recent development," IEEE Transactions on Electronics Packaging Manufacturing **26**, 141–149 (2003).

[29] D. Tennant and A. Bleier, "Electron beam lithography of nanostructures," Reference Module in Materials Science and Materials Engineering (2016), 10.1016/b978-0-12-803581-8.09255-9.

[30] S. Hu, O. Dyck, H. Chen, Y.-c. Hsiao, B. Hu, G. Duscher, M. Dadmun, and B. Khomami, "The impact of selective solvents on the evolution of structure and function in solvent annealed organic photovoltaics," RSC Adv. **4**, 27931–27938 (2014).

[31] R. Tait, T. Smy, and M. Brett, "Modelling and characterization of columnar growth in evaporated films," Thin Solid Films **226**, 196–201 (1993).

[32] P. N. Shankar and M. D. Deshpande, "Fluid mechanics in the driven cavity," Annual Review of Fluid Mechanics **32**, 93–136 (2000).

[33] S. Taneda, "Visualization of separating stokes flows," Journal of the Physical Society of Japan **46**, 1935–1942 (1979).

[34] H. Suhl, "Ferromagnetic resonance in nickel ferrite between one and two kilomegacycles," Physical Review **97**, 555–557 (1955).

[35] J. Smit and H. G. Beljers, "Ferromagnetic resonance absorption in $BaFe_{12}O_{19}$, a highly anisotropic crystal," Philips Res. Rep. **10**, 113–130 (1955).

[36] L. Baselgia, M. Warden, F. Waldner, S. L. Hutton, J. E. Drumheller, Y. Q. He, P. E. Wigen, and M. Maryško, "Derivation of the resonance frequency from the free energy of ferromagnets," Physical Review B **38**, 2237–2242 (1988).

[37] J. Smit and H. Wijn, "Physical properties of ferrites," Advances in Electronics and Electron Physics , 69–136 (1954).

[38] A. H. Morrish, "The physical principles of magnetism," (2001), 10.1109/9780470546581.

[39] A. Smith, K. K. Nielsen, D. V. Christensen, C. R. H. Bahl, R. Bjørk, and J. Hattel, "The demagnetizing field of a nonuniform rectangular prism," Journal of Applied Physics **107**, 103910 (2010).

[40] L. Kraus, "The demagnetization tensor of a cylinder," Czechoslovak Journal of Physics **23**, 512–519 (1973).

[41] B. A. Kalinikos and A. N. Slavin, "Theory of dipole-exchange spin wave spectrum for ferromagnetic films with mixed exchange boundary conditions," Journal of Physics C: Solid State Physics **19**, 7013–7033 (1986).

[42] R. Skomski, A. Kashyap, Y. Qiang, and D. J. Sellmyer, "Exchange through nonmagnetic insulating matrix," Journal of Applied Physics **93**, 6477–6479 (2003).

[43] R. Skomski, "Nanomagnetic scaling," Journal of Magnetism and Magnetic Materials **272-276**, 1476–1481 (2004).

[44] R. Moreno, R. F. L. Evans, S. Khmelevskyi, M. C. Muñoz, R. W. Chantrell, and O. Chubykalo-Fesenko, "Temperature-dependent exchange stiffness and domain wall width in Co," Physical Review B **94** (2016), 10.1103/physrevb.94.104433.

[45] A. Vansteenkiste, J. Leliaert, M. Dvornik, M. Helsen, F. Garcia-Sanchez, and B. Van Waeyenberge, "The design and verification of MuMax3," AIP Advances **4**, 107133 (2014).

[46] S. S. Kalarickal, P. Krivosik, M. Wu, C. E. Patton, M. L. Schneider, P. Kabos, T. J. Silva, and J. P. Nibarger, "Ferromagnetic resonance linewidth in metallic thin films: Comparison of measurement methods," Journal of Applied Physics **99**, 093909 (2006).

[47] B. Heinrich, J. F. Cochran, and R. Hasegawa, "Fmr linebroadening in metals due to two-magnon scattering," Journal of Applied Physics **57**, 3690–3692 (1985).

[48] M. Balinskiy, B. Mongolov, D. Gutierrez, H. Chiang, A. Slavin, and A. Khitun, "Perpendicularly magnetized YIG-film resonators and waveguides with high operating power," AIP Advances **7**, 056612 (2017).

[49] A. V. Chumak, A. A. Serga, and B. Hillebrands, "Magnon transistor for all-magnon data processing," Nature Communications **5** (2014), 10.1038/ncomms5700.

[50] L. Cornelissen, J. Liu, B. van Wees, and R. Duine, "Spin-current-controlled modulation of the magnon spin conductance in a three-terminal magnon transistor," Physical Review Letters **120** (2018), 10.1103/physrevlett.120.097702.

[51] R. G. E. Morris, A. F. van Loo, S. Kosen, and A. D. Karenowska, "Strong coupling of magnons in a YIG sphere to photons in a planar superconducting resonator in the quantum limit," Scientific Reports **7** (2017), 10.1038/s41598-017-11835-4.

[52] X. Zhang, C.-L. Zou, L. Jiang, and H. X. Tang, "Strongly coupled magnons and cavity microwave photons," Physical Review Letters **113** (2014), 10.1103/physrevlett.113.156401.

[53] R. C. LeCraw, E. G. Spencer, and C. S. Porter, "Ferromagnetic resonance line width in yttrium iron garnet single crystals," Physical Review **110**, 1311–1313 (1958).

Low-Damping Ferromagnetic Resonance in Electron-Beam Patterned, High-Q Vanadium Tetracyanoethylene Magnon Cavities

Andrew Franson,[1] Na Zhu,[2] Seth Kurfman,[1] Michael Chilcote,[1] Denis R. Candido,[3,4] Kristen S. Buchanan,[5] Michael E. Flatté,[3,4] Hong X. Tang,[2] and Ezekiel Johnston-Halperin[1]

[1)]*Department of Physics, The Ohio State University, Columbus, Ohio 43210, USA*

[2)]*Department of Electrical Engineering, Yale University, New Haven, Connecticut 06511, USA*

[3)]*Department of Physics and Astronomy, University of Iowa, Iowa City, Iowa 52242, USA*

[4)]*Pritzker School of Molecular Engineering, University of Chicago, Chicago, Illinois 60637, USA*

[5)]*Department of Physics, Colorado State University, Fort Collins, Colorado 80523, USA*

PATTERNING AND MEASUREMENT METHODS

Patterning and Growth

$V[TCNE]_x$ bars and disks are patterned on commercially available C-plane polished sapphire (Al_2O_3) via electron-beam lithographic techniques. The substrates are cleaned with a solvent chain of acetone, methanol, isopropanol (IPA), and deionized water (DI water) followed by a 20 minute ultraviolet ozone clean (UVOC) in a UVOCS T10x10/OES to degrease and remove organic contaminants. A 400 nm layer of MMA (8.5) MAA EL 11 (P(MMA-MAA)) is spun on at 2000 rpm for 45 seconds then soft baked at 180 °C for 300 seconds. A 140 nm layer of 495PMMA A6 (PMMA) is then spun on at 2000 rpm for 45 seconds then soft baked at 180 °C for 60 seconds. A 10 nm thick layer of aluminum is deposited via thermal deposition at 1×10^{-6} Torr. The electron-beam patterning of the PMMA/P(MMA-MAA) bilayer is performed on a FEI Helios Nanolab 600 Dual Beam Focused Ion Beam/Scanning Electron Microscope with the assistance of Nanometer Pattern Generation System (NPGS) software. Development of the written pattern is achieved with Microposit MF-319 for 40 seconds, DI water for 20 seconds, MF-319 for 40 seconds, DI water for 20 seconds, Microchem MIBK:IPA (1:3) for 60 seconds, IPA for 20 seconds, DI water for 20 seconds. That is followed by a 120 second hard bake at 100 °C. A 3 nm thick layer of aluminum is then deposited in the same system as the prior 10 nm layer to prevent outgassing of the PMMA/P(MMA-MAA) bilayer during $V[TCNE]_x$ deposition. The sample is oxidized and cleaned with a 10-minute UVOC. This oxidizes the surface of the 3 nm aluminum layer and removes potential small sources of contamination from the growth surfaces. Growth of $V[TCNE]_x$ is described in previous work.[1] After transfer of the films from the growth glovebox to the liftoff glovebox, liftoff is performed in dichloromethane. For the feature sizes and thicknesses used here, liftoff occurred in a few minutes with gentle agitation from a Pasteur pipette.

Microwave Measurements

Angle-resolved ferromagnetic resonance (FMR) measurements are done with a Bruker electron paramagnetic resonance spectrometer with an X-band bridge and 10 kOe electromagnet. Before measurement, the $V[TCNE]_x$ samples are sealed into a quartz tube with a ceramic holder that aligns the normal plane of the sample. Between each scan, the microwave frequency is tuned between 9 and 10 GHz to match the resonant frequency of the loaded cavity. The frequency is fixed and

measurements are then performed by sweeping the static field with 200 μW of applied microwave power and a modulation field of 0.1 Oe. The quartz tube has a pointer fixed to it, allowing for alignment within 0.5 degrees of the sample with respect to a custom made goniometer. The larger error of ± 2 degrees seen in Fig. 3(d) comes from the initial aligning the goniometer with the in-plane (IP, $\theta = 90$) orientation of the $V[TCNE]_x$ film. The IP orientation is taken to be the point where the resonance field is at its minimum.

Frequency-resolved microwave measurements are done with a broadband ferromagnetic resonance (BFMR) setup with a B4003-8M-50 microstrip test board from Southwest Microwave that is sourced by an Agilent N5222A vector network analyzer (VNA), transduced via a Krytar 203BK Schottky diode, and measured with an Ametek 7265 Dual Phase DSP lock-in amplifier. The microstrip is positioned inside a 10 kOe electromagnet in the out-of-plane (OOP, $\theta = 0$) field geometry. Measurements are performed with an input power of -10 dBm and a modulation field of roughly 0.1 Oe oscillating at 577 Hz.

NUMERICAL MODELING

Micromagnetic simulations are done to gain insight into the measured FMR spectra. The micromagnetic simulations are done using MuMax3[2] with the following parameters for the $V[TCNE]_x$: saturation magnetization $4\pi M_s = 76.57\,G$ (6093 A/m), exchange constant $A_{ex} = 2.2 \times 10^{-10}\,erg/cm$ ($2.2 \times 10^{-15}\,J/m$), and a damping parameter of $\alpha = 0.0001$, where α is larger than the smallest measured damping value for $V[TCNE]_x$ and was chosen to ensure that the simulations would converge in a reasonable amount of time. Cells of 40 x 40 x 4.6875 nm^3 are used. Selected simulations are repeated with smaller cells with similar results because the 40 nm cell sizes are still small compared to the wavelengths of the spin-wave modes. A_{ex} is determined by fitting the mode spacing of the thickness confined modes from the OOP spectra of the disks blue anisotropy curves in Fig. 3(c). Fitting is done to theory from Kalinikos et al.[3] and is shown in Fig. 3(e). Fitting for fully pinned and fully unpinned geometries yielded the same value for A_{ex}.

The simulations are done with the static field, H_{bias}, applied OOP. The field magnitudes are chosen to result in a resonance frequency near 9.83 GHz to be similar to the measurement frequency used in the experiments. The structures are relaxed in the presence of H_{bias} and a small additional field H_{dynam} of roughly 50 Oe, chosen such that the spins tilt by about 1% from the static equilibrium position, is applied in the x-direction. The dynamics are monitored as a function of time after removing H_{dynam} and the simulated spectra are obtained by taking the Fourier transforms of the x-component of the magnetization for each run. Mode profiles are calculated for selected peaks in the spectra by running driven simulations at the selected resonance frequency and extracting the spin distributions as a function of time for a full period after the simulation has reached a steady state.

Since the pinning of the structures is unknown and the exact profile is uncertain, a matrix of different combinations of pinning and cross-sectional profile is investigated. Three geometries are considered based on the growth characteristics of the bar in Fig. 1(b, c), a cylindrical disk; a lens-shaped, circular disk with a spherically-curved top surface and flat bottom surface (spherical cap); and a disk with a 1 μm wide ramp from the outer rim to the inner rim, Fig. S1. For each of these geometries, simulations with no pinning of surface spins, perfect pinning on the top surface, perfect pinning on the bottom surface, and perfect pinning on both the top and bottom surfaces is considered. To compare the experimental spectra with the simulations, we considered the prevalence of the thickness modes and the shape of the strongest peak. The mode spacing does

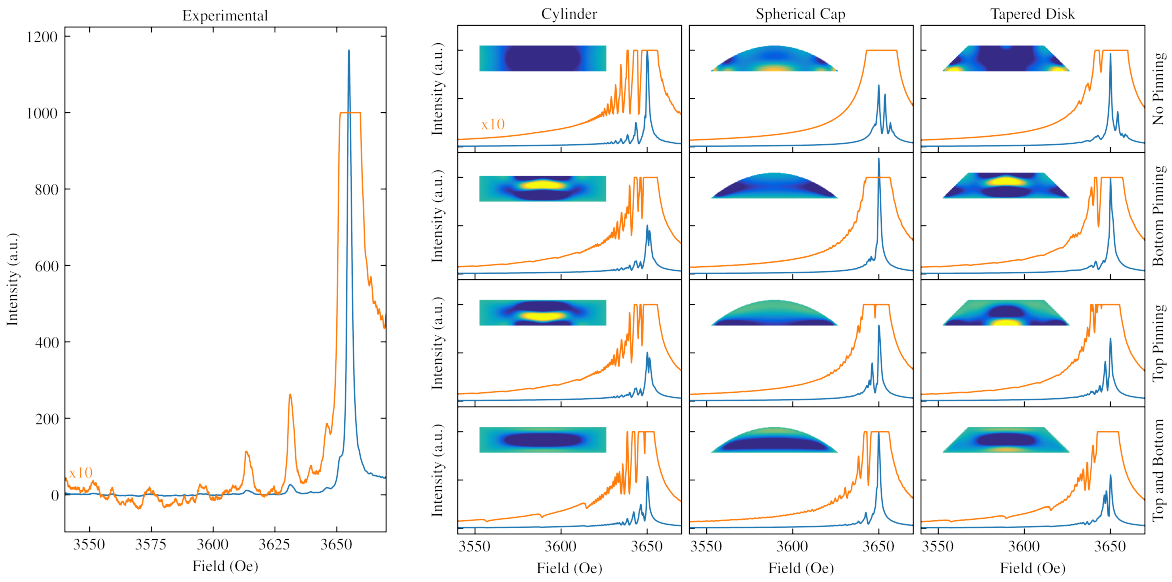

FIG. S1. Left, experimental data of the 9.83 GHz OOP FMR scan of the array of 5 µm disks. Right, array of the different simulated geometries considered in this study. Blue lines represent the full data and the orange lines are the full data multiplied by 10 and truncated to better show low-intensity, low-field behavior. Mode maps of the vertical cross-sections of the mode maps at the disk center for the largest amplitude peak for each simulated geometry are shown in the upper left of each plot, where dark blue (dark), green (medium), and yellow (light) represent negative, zero, and positive motion, respectively, at an instant of time. These are quantized standing modes.

not change appreciably with the disk shape (taper vs. lens), and agrees well with the calculations of the mode spacing for an unpatterned thin film. The spherical cap used for the lens-type simulations leads to almost complete suppression of the thickness modes for all of the pinning conditions, which is not consistent with the experimental spectrum. The strongest peak in the data is smoother than the jagged combo-like structure of the main peak of the cylindrical simulations that occurs due to the radial modes. The two simulations that are the closest to the experimental data are the tapered-disk simulations with top/bottom and bottom-only pinning. The even modes show up almost as strongly as the odd modes for bottom-only pinning, whereas only the odd modes are present for top/bottom pinning. As show in Fig. 3(e), resonance peaks that correspond to even thickness modes are present but weak compared to the odd modes, which suggests that both surfaces are pinned but that pinning is imperfect on one of the two surfaces, likely the top.

FITTING METHODS

All fitting is performed in Python with the emcee package[4] within the lmfit package.[5]

Cavity FMR Angular Anisotropy Fitting

Fitting of the red anisotropy curves in Fig. 3(d) are all performed with a modified Eq 2. Squaring both sides and collecting factors of H yields

$$\left(\frac{\omega}{\gamma}\right)^2 = H^2 + H \times 4\pi M_s \left(-N_{IP}\cos(2\theta) - N_{IP}\cos(\theta)^2 - N_{OP}\cos(2\varphi)\right) + 16\pi^2 M_s^2 \left(N_{IP}^2\cos(\theta)^2 + N_{IP}N_{OP}\cos(2\theta)\cos(2\varphi) - N_{OP}^2\cos(\theta)^2\cos(\varphi)^2\sin(\varphi)^2\right), \quad \text{(S.1)}$$

solving for H then yields

$$H = \frac{-b \pm \sqrt{b^2 - 4ac}}{2a} \quad \text{(S.2)}$$

where

$$a \equiv 1, \quad \text{(S.3a)}$$

$$b \equiv 4\pi M_s(-N_{IP}\cos(2\theta) - N_{IP}\cos(\theta)^2 - N_{OP}\cos(2\varphi)), \quad \text{(S.3b)}$$

$$c \equiv 16\pi^2 M_s^2 \left(N_{IP}^2\cos(\theta)^2 + N_{IP}N_{OP}\cos(2\theta)\cos(2\varphi) - N_{OP}^2\cos(\theta)^2\cos(\varphi)^2\sin(\varphi)^2\right) - \left(\frac{\omega}{\gamma}\right)^2. \quad \text{(S.3c)}$$

To account for deviations from high-symmetry directions, θ and φ are parameterized in terms of a new parameter, t. This parameterization allows for fitting through a path along any great circle of the unit sphere by using the expression

$$\vec{v_1} = \sin(\theta_1)\cos(\varphi_1)\hat{x} + \sin(\theta_1)\sin(\varphi_1)\hat{y} + \cos(\theta_1)\hat{z} \quad \text{(S.4a)}$$

$$\vec{v_2} = \sin(\theta_2)\cos(\varphi_2)\hat{x} + \sin(\theta_2)\sin(\varphi_2)\hat{y} + \cos(\theta_2)\hat{z} \quad \text{(S.4b)}$$

$$\eta = \arccos(\vec{v_1}\cdot\vec{v_2}) \quad \text{(S.4c)}$$

$$\vec{v_m} = \frac{\sin(\eta(1-t))\vec{v_1} + \sin(\eta t)\vec{v_2}}{\sin(\eta)} \quad \text{(S.4d)}$$

where $\vec{v_m}$ points to a location on the great circle that intersects $\vec{v_1}$ and $\vec{v_2}$. The location is determined by the parameter t which steps from $t_i = 0$ to $t_f = \frac{\pi}{\eta}$ in steps of $t_{step} = \frac{t_f - t_i}{18}$ to produce 10° steps from 0° to 180°.

This correction is only necessary for the bar sample scanned IP to OOP with the applied field perpendicular to the bar axis (red diamonds in Fig. 3(d)). A path traveling from the IP position ($\theta_1 = 90°$, $\varphi_1 = 90°$) to a position 10° away from OOP ($\theta_2 = 10°$, $\varphi_2 = 90°$) is required to accurately describe the data. This corresponds to an initial θ offset in the x-direction while sweeping θ in the y-direction and explains why the red-diamond curve does not kiss the red-circle and red-square curves at exactly one point.

Broadband FMR Linewidth Fitting

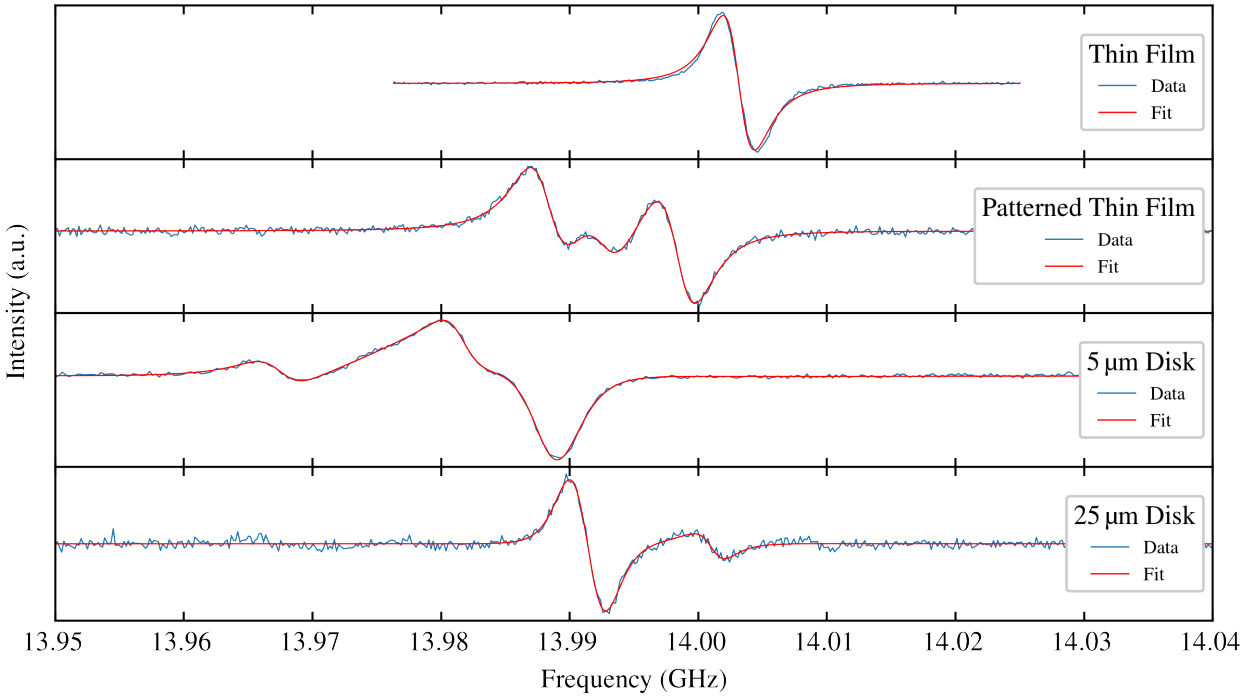

FIG. S2. Representative single scans of various $V[TCNE]_x$ features ranging from an unpatterned thin film to a 5 μm diameter disk array. All scans are done in the OOP ($\theta = 0$) geometry. All growths were 1-hour long, resulting in a 300 nm thick film for the 5 μm film and 400 nm thickness for the rest. The patterned thin film is a 2 mm by 2 mm patterned patch of $V[TCNE]_x$. The linewidth is extracted from the fit to the furthest right lorentzian except for the 25 μm disks where the linewidth is extracted from the largest peak.

Figure S2 shows representative linescans from the BFMR measurement setup. The spectra are fit well by a combination of several lorentzian derivatives. Each lorentzian derivative function has antisymmetric (absorptive) and symmetric (dispersive) components[6] represented by

$$L'_{abs}(f) = \frac{a\Gamma^3(f-f_0)}{\left(\Gamma^2+4(f-f_0)^2\right)^2}, \tag{S.5a}$$

$$L'_{disp}(f) = \frac{-d\Gamma^2\left(\Gamma^2-4(f-f_0)^2\right)}{\left(\Gamma^2+4(f-f_0)^2\right)^2}, \tag{S.5b}$$

so each derivative lorentzian in the fit is represented by

$$L'_{total}(f) = \frac{a\Gamma^3(f-f_0)}{\left(\Gamma^2+4(f-f_0)^2\right)^2} - \frac{d\Gamma^2\left(\Gamma^2-4(f-f_0)^2\right)}{\left(\Gamma^2+4(f-f_0)^2\right)^2} \tag{S.6}$$

where a is the height of the derivative of the absorptive component, d is the height of the derivative of the dispersive component, Γ is the full-width at half-maximum of the lorentzian, f is the independent variable, and f_0 is the peak of the lorentzian.

ANALYTIC RESONANT FIELD CALCULATIONS

Here we find an analytical expression for the spin-wave (or magnetostatic mode) resonant fields for a normally magnetized cylinder with thickness d and radius R. We first solve Maxwell's equations within the magnetostatic regime. Application of the proper boundary conditions at $z = \pm\frac{d}{2}$, the top and bottom surfaces of our cylinder, yields the following transcendental equations[7,8]

$$\tan(k_i d) = 2\frac{k_o k_i}{k_i^2 - k_o^2}, \tag{S.7}$$

$$\frac{ik_i}{\sqrt{1+\kappa}} = k_o, \tag{S.8}$$

where k_o and k_i are the in-plane and out-of-plane wave vectors, respectively, and $\kappa = \frac{\Omega_H}{\Omega_H^2 - \Omega^2}$, with $\Omega_H = \frac{H + M_s\lambda_{ex}\left(k_i^2 + k_0^2\right)}{M_s}$, $\lambda_{ex} = \frac{2A_{ex}}{\mu_0 M_s^2}$ and $\Omega = \frac{\omega}{\gamma M_s}$. An analytic expression for the resonant spin-wave fields is then obtained from the Maxwell's equation coupled to the Laudau-Lifshitz equation, with the additional assumption that the magnetization is pinned at $r = R$, which yields[7,8]

$$J_{m-1}(k_o R) = 0, \tag{S.9}$$

$$\rightarrow k_{o,m-1}^n = \frac{\beta_{m-1}^n}{R}, \tag{S.10}$$

where β_{m-1}^n is the n$^{\text{th}}$-zero of the Bessel function of order $m-1$. Now using Eq. S.8 and Eq. S.10 we obtain[8] the following expression for the spin-wave resonant fields

$$B_{nml}^z \approx \mu_o\frac{\omega}{\gamma} + \mu_o M_s - \frac{2A_{ex}}{M_s}\left[k_{i,nml}^2 + \left(\frac{\beta_{m-1}^n}{R}\right)^2\right] - \frac{\mu_o M_s}{2\left(1 + \frac{k_{i,nml}^2 R^2}{\left(\beta_{m-1}^n\right)^2}\right)} - \frac{\mu_o (M_s)^2}{8\frac{\omega}{\gamma}\left(1 + \frac{k_{i,nml}^2 R^2}{\left(\beta_{m-1}^n\right)^2}\right)^2}, \tag{S.11}$$

assuming $\frac{\omega}{\gamma} \gg M_s\left[2\left(1 + \frac{k_{i,nml}^2 R^2}{\left(\beta_{m-1}^n\right)^2}\right)\right]^{-1}$. The indices n, m and l represent the radial, angular, and thickness mode numbers, respectively. The resonant fields in Eq. S.11 are derived using the SI electromagnetic equations and B_{nml}^z has units of Tesla (T). To obtain the resonant fields H_{nml}^z in Oersted (Oe) unit, the values obtained from Eq. S.11 should be multiplied by 1×10^4 Oe/T.

Eq. S.11 does not account for the demagnetization field. A good match with the experimental data is obtained using the approached described in Kakezei[9] that considers an effective demagnetization per mode N_{nml}. To account for the effect of the demagnetization field, we substitute $M_s \rightarrow M_s N_{nml}$ with $N_{nml} < 1$. Fig. S3 shows the resonant fields found using Eq. S.11 for $N_{nml} \in [0.865 - 0.925]$[8–10] for different d. The best match with the experimental data is for

$d = 250$ nm. This is smaller than the nominal thickness of the $V[TCNE]_x$ disks used in the experiment (300 nm), which we attribute to the fact that the lens shape leads to a smaller effective thickness. Like the simulations, the analytical calculations also predict a much closer spacing for the radial modes as compared to the thickness-quantized modes (not shown).

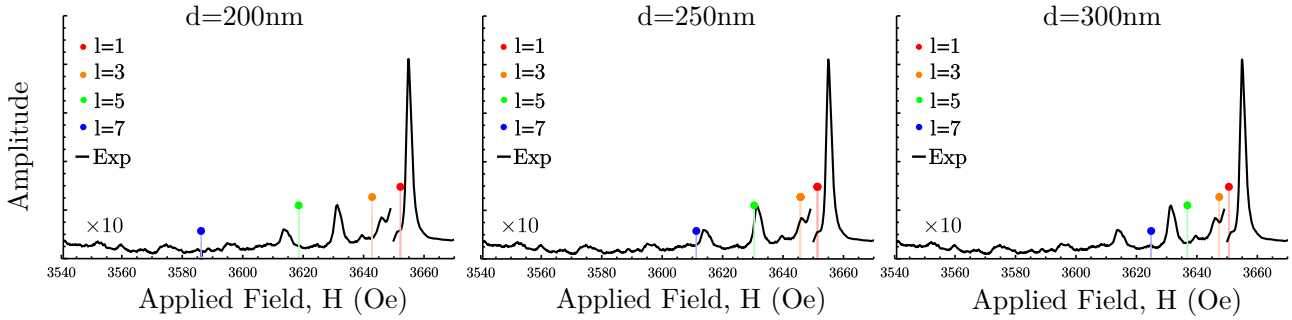

FIG. S3. Plot of the resonant fields for the first five thickness modes $l = 1,3,5,7$ for the angular and radial modes $m = 1$ and $n = 1$ a) $d = 200$nm, b) $d = 250$nm and c) $d = 300$nm. For all three plots, $A = 2.2 \times 10^{-10}$ erg/cm, $M_s = 76.57$ G, $N_{nml} \in [0.865 - 0.925]$, $\omega = 9.83$ GHz, $\gamma = 2.73 \times 10^6$ MHz/Oe, and $R = 2500$ nm. The black line shows the experimental spectrum obtained for the $V[TCNE]_x$ cylinder for the OOP field orientation ($\theta = 0$, $\varphi = 0$).

REFERENCES

[1]H. Yu, M. Harberts, R. Adur, Y. Lu, P. C. Hammel, E. Johnston-Halperin, and A. J. Epstein, "Ultra-narrow ferromagnetic resonance in organic-based thin films grown via low temperature chemical vapor deposition," Applied Physics Letters **105**, 012407 (2014).

[2]A. Vansteenkiste, J. Leliaert, M. Dvornik, M. Helsen, F. Garcia-Sanchez, and B. Van Waeyenberge, "The design and verification of MuMax3," AIP Advances **4**, 107133 (2014).

[3]B. A. Kalinikos and A. N. Slavin, "Theory of dipole-exchange spin wave spectrum for ferromagnetic films with mixed exchange boundary conditions," Journal of Physics C: Solid State Physics **19**, 7013–7033 (1986).

[4]D. Foreman-Mackey, D. W. Hogg, D. Lang, and J. Goodman, "emcee: The MCMC hammer," Publications of the Astronomical Society of the Pacific **125**, 306–312 (2013).

[5]M. Newville, T. Stensitzki, D. B. Allen, and A. Ingargiola, "LMFIT: Non-linear least-square minimization and curve-fitting for Python," (2014).

[6]S. S. Kalarickal, P. Krivosik, M. Wu, C. E. Patton, M. L. Schneider, P. Kabos, T. J. Silva, and J. P. Nibarger, "Ferromagnetic resonance linewidth in metallic thin films: Comparison of measurement methods," Journal of Applied Physics **99**, 093909 (2006).

[7]M. Sparks, "Magnetostatic modes in an infinite circular disk," Solid State Communications **8**, 731–733 (1970).

[8]D. R. Candido and M. E. Flatté, to be published.

[9]G. N. Kakazei, P. E. Wigen, K. Y. Guslienko, V. Novosad, A. N. Slavin, V. O. Golub, N. A. Lesnik, and Y. Otani, "Spin-wave spectra of perpendicularly magnetized circular submicron dot arrays," (2004).

[10]S. V. Nedukh, S. I. Tarapov, D. P. Belozorov, A. A. Kharchenko, V. O. Golub, I. V. Kilimchuk, O. Y. Salyuk, E. V. Tartakovskaya, S. A. Bunyaev, and G. N. Kakazei, "Standing spin waves in perpendicularly magnetized circular dots at millimeter waves," Journal of Applied Physics **113**, 17B521 (2013).

[11]I. S. Maksymov and M. Kostylev, "Broadband stripline ferromagnetic resonance spectroscopy of ferromagnetic films, multilayers and nanostructures," Physica E: Low-dimensional Systems and Nanostructures **69**, 253–293 (2015).